

Analysis of a single-mode waveguide at sub-terahertz frequencies as a communication channel

Marc Westig,^{1,2,a)} Holger Thierschmann,¹ Allard Katan,¹ Matvey Finkel,¹ and Teun M. Klapwijk¹

¹⁾*Kavli Institute of NanoScience, Delft University of Technology, Lorentzweg 1, 2628 CJ Delft, The Netherlands*

²⁾*Fachbereich Physik, Freie Universität Berlin, Arnimallee 14, 14195 Berlin, Germany*

We study experimentally the transmission of an electro-magnetic waveguide in the frequency range from 160 to 300 GHz. Photo-mixing is used to excite and detect the fundamental TE_{10} mode in a rectangular waveguide with two orders-of-magnitude lower impedance. The large impedance mismatch leads to a strong frequency dependence of the transmission, which we measure with a high-dynamic range of up to 80 dB, and with high frequency-resolution. The modified transmission function is directly related to the information rate of the waveguide, which we estimate to be about 1 bit per photon. We suggest that the results are applicable to a Josephson junction employed as a single-photon source and coupled to a superconducting waveguide to achieve a simple on-demand narrow-bandwidth free-space number-state channel.

I. INTRODUCTION

An important problem in communication technology is the transmission of a coded message, from an initial point *via* a channel to a final point, with minimal error in receiving and decoding the message. Electro-magnetic transmission lines, like an optical fibre or a waveguide, are attractive as a communication channel, because compared to free space, they minimize the radiative information loss. The effectiveness of a channel, in terms of the information rate, is quantified by the channel capacity, measured in bits per second or in bits per photon.¹⁻³ The most effective way of using a waveguide is by implementing a "one quantum - one bit - one mode" strategy as introduced by Caves and Drummond¹. Here, we analyze experimental results on the transmission of a waveguide at sub-terahertz (THz) frequencies in the context of this information communication-effectiveness.

Three-dimensional (3D) waveguides and cavities have recently entered the field of quantum-information technology in the form of superconducting cavities, which show at the frequencies around 10 GHz the lowest (dissipative) loss to date^{4,5} and, therefore, support a superior qubit operation. The reason for the low loss is the minimal relative energy stored in surface defects in 3D cavities,⁶ compared to other technologies like planar (2D) resonators or conductors.⁷ For a 3D cavity, the relative energy loss in surface defects scales inversely proportional to its size,⁵ which is also dependent on the propagating mode, because of the mode-dependent current distribution at the cavity walls. This type of technology has been developed many years ago in the field of astronomical detectors⁸ for applications at significantly higher frequencies. Developed for the astronomically important range of hundreds of GHz and for other sophisticated 3D sub-mm waveguide circuits,⁹ the technology appears suitable for use in quantum networks as well.

In previous work, isotropic dispersion relations have been included in the description of the communication channel. In this case the signal group velocity along the channel at frequency f scales with all spatial dimensions along the channel, as noted by Caves and Drummond¹ and, hence, the information rate is not modified by this isotropic dispersion. In the present work we identify that the frequency-dependent transmission of a single-mode rectangular waveguide carries directly over to the channel capacity. We quantify this by analytic expressions and numerical modeling. It shows that it is caused by the high-impedance source and detector, coupled to the two orders-of-magnitude lower impedance of the fundamental TE_{10} mode of the waveguide (using a waveguide of length $l = 39.6$ (79.2) mm, *i.e.* which is 33 (66)-times longer than the center wavelength). As a result, for a single frequency-multiplexed coherent-state channel, the information rate varies up to a factor of about 2 over the transmission bandwidth of 210 to 300 GHz.

The paper is organized as follows. Section II describes our experimental method and setup. In Sec. III A and III B the electro-magnetic modeling results of the diagonal horn antennas and the waveguides of our setup are provided. In a second step we connect the modeling results to the optical properties of the used photo-mixers (Sec. III C), *i.e.* their characteristic wave impedance, using the ABCD-matrix formalism to obtain a complete model. The measured response is presented and analyzed in Sec. IV. In Sec. V we summarize theoretical expressions for the channel capacity, in which the effect of the frequency-dependent transmission through our diagonal-horn antenna/waveguide assembly on the information rate becomes clear. It includes essential details of the capacity for two types of communication channels, a coherent-state channel and a number-state channel. Section VI discusses experimentally realized Josephson circuits which together with superconducting waveguides are well suited for implementing in free-space the concepts discussed theoretically in Sec. V. We conclude our work in Sec. VII.

^{a)}Electronic mail: mpwestig@gmail.com

II. EXPERIMENTAL SETUP

In Fig. 1 we show a sketch of a standard open rectangular waveguide and the standard prediction for the transmission using the analytical theory presented in Bayer¹⁰. Our aim is to evaluate experimentally this prediction for the sub-THz frequency range. The shown predictions are for a lossless and impedance-matched waveguide, the step-function, and for two impedance-matched waveguides of different lengths including the loss in the material. A longer waveguide naturally has a lower transmissivity because of the loss of signal occurring over the length of the waveguide. An experimental test of this prediction is currently possible because of the availability of high quality waveguides and continuously tunable sources. The full experimental setup is shown in Fig. 2(a). The central element is the waveguide, like schematically shown in Fig. 1(a), and represented in detail in Fig. 2(d). A free space sub-THz electromagnetic wave enters a diagonal horn, travels through the waveguide, and is radiated out again from a diagonal horn. The horns and waveguide are made of the same material, CuTe, using present-day computer-controlled machining technology. The frequency-tunable electromagnetic signal, in the appropriate frequency range of 160 to 300 GHz, is generated and detected by superimposing the outputs of two 780 nm distributed feedback (DFB) lasers in a beam combiner (BC) and illuminating two GaAs photo-mixers connected at the output of the beam combiner via polarization maintaining fibers (PMF), with one photo-mixer acting as coherent THz source (S) and the second one as coherent THz detector (D).¹¹ The incident laser power on each photo-mixer is approximately 30 mW. The desired frequency of the THz electro-magnetic signal is set by adjusting the difference frequency between the two DFB lasers. Optimal coupling between all optical elements is achieved by arranging the setup according to the distances summarized in Sec. III C.

Each photo-mixer consists of a metallic two-electrode log-spiral circuit, patterned on a GaAs chip. The non-patterned side of the GaAs chip is glued on a silicon lens, employed for Gaussian beam formation. The laser spot from the optical fiber is focussed on the feedpoint of the log-spiral circuit. The relevant equivalent circuits are drawn in Figs. 2(b) and (c). The source photo-mixer is biased by a 39.6 kHz modulated on/off voltage of $V_{dc} = 6V$, facilitating a lock-in detection of the measured signals. A detailed overview of the GaAs mixer-technology is provided in the reviews by Preu *et al.*¹², Brown¹³ and Saeedkia¹⁴.

We analyze the emitted THz field from the diagonal horn as follows. The THz electric field component received by the detector leads to an ac-voltage drop across an interdigitated capacitor of the detector with a frequency equal to the laser detuning f . Together with the laser-induced impedance modulation with the same frequency, but in general with a different phase, a co-

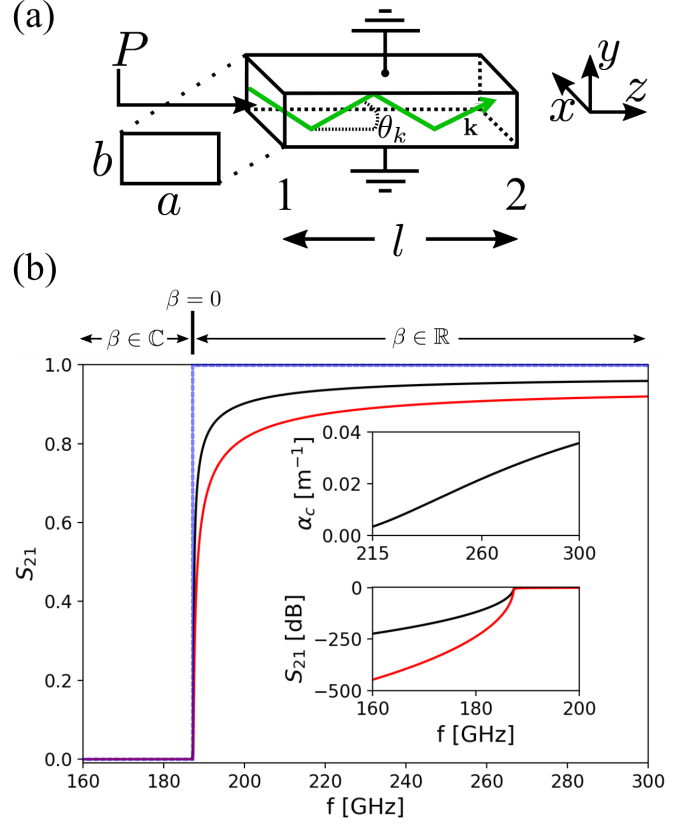


FIG. 1. (a) Sketch of an ideal input/output impedance matched waveguide, assuming $a = 800 \mu\text{m}$ and $b = a/2$. The signal power P is injected at the input 1 and reaches the output 2. If only the fundamental mode is excited, the polar angle θ_k quantifies via the relation $c_0 \cos(\theta_k)$ the longitudinal group velocity in the waveguide. (b) Calculated transmission from port 1 to port 2 for two different lengths $l = 39.6 \text{ mm}$ (black) and $l = 79.2 \text{ mm}$ (red) using the standard analytical theory presented in Bayer¹⁰. The blue line is for an idealized response without loss as expected for a superconducting waveguide, as long as the photon energy is below the value of the superconducting energy gap. For frequencies lower than the waveguide cut-off frequency $f < f_{\min} = c_0/(2a)$, the propagation constant for the fundamental mode, β , is complex-valued, meaning that only evanescent waves exist in the waveguide. Here, $k_z = 2\pi/\lambda_g$ is the wavevector with λ_g being the guide wavelength. For $f_{\min} < f < 2f_{\min}$, the propagation constant is real-valued and a traveling wave is launched in the waveguide characterized by the fundamental TE_{10} mode. The upper inset in (b) shows the calculated conductor loss α_c for the material CuTe, used in the experiment and also for the calculations in this figure (red, black) as a function of frequency. The lower inset shows a magnified view of the evanescent-wave transmission range on a logarithmic scale.

herent dc-photocurrent, $I_{dc}(f)$, flows in the positive or negative direction (dependent on the phase) across the feedpoint of the log-spiral circuit. The dc-photocurrent induces a voltage drop across the detection impedance R_{ph} (Fig. 2(c)) which is amplified while preserving its sign in a trans-impedance amplifier (type PDA-S) with

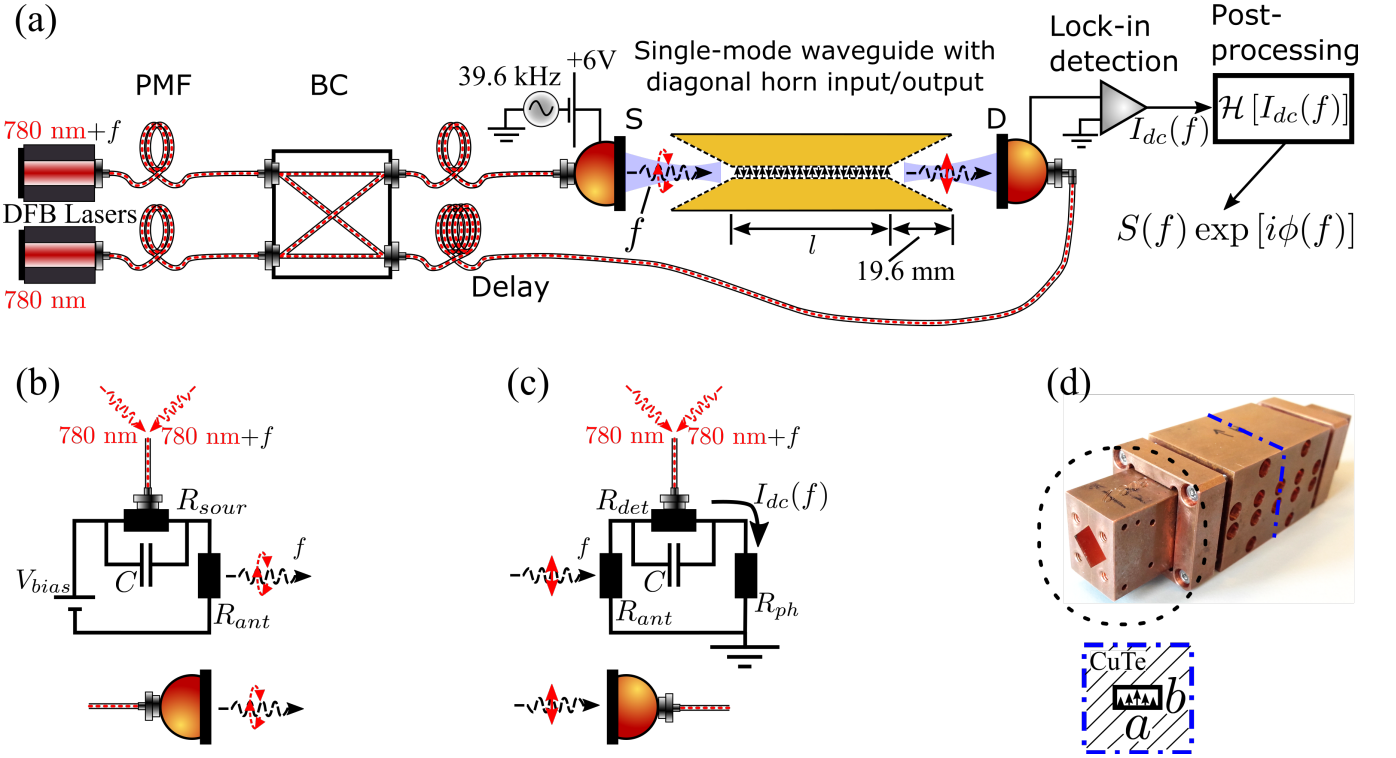


FIG. 2. (a) Experimental setup. PMF = polarization maintaining fibres (Thorlabs GmbH), BC = beam combiner and S/D = source/detector (TOPTICA Photonics AG).¹¹ The light blue profile indicates the Gaussian beam shape of the source and detector which is coupled to the diagonal-horn aperture. The vertical red arrow at the output shows the linear polarization of the radiated field received by the detector. The polarization change occurs due to the electro-magnetic field distribution in the waveguide, sketched in (d). (b) and (c) indicate the electrical-circuit model of the source and detector. (d) Fabricated CuTe waveguide with mounted diagonal-horn antennas of the same material. The blue dash-dotted rectangle indicates a cut through the waveguide, sketching the hollow waveguide channel with length a and width $b = a/2$ and the linearly polarized electrical field lines, parallel to the b -side.

a bandwidth of 0-1 MHz. Each data-point is then integrated over 500 ms. This detection scheme resembles a homodyne detector at THz frequencies with a high-dynamic range up to 80 dB¹¹ like described by Roggenbuck *et al.*¹⁵. A benefit of this scheme is that it measures the transmitted amplitude rather than only the transmitted power. In this work we use only the instantaneous amplitude (envelope function $\propto \sqrt{P}$) of the Hilbert transformation of $I_{dc}(f)$, Eq. (1), for comparison with our theoretical model:

$$\mathcal{I}_{dc}(f) = I_{dc}(f) + i\mathcal{H}[I_{dc}(f)] = S(f) \exp[i\phi(f)] . \quad (1)$$

Here, $\mathcal{H}(\dots)$ is the Hilbert transformation,¹⁶ $\phi(f)$ the instantaneous phase of the signal and $S(f)$ is the instantaneous amplitude which we show in Figs. 5 and 6 as experimental data.

Since the interplay between generation and detection of the sub-THz signal plays a crucial role in our work, we address both in a bit more detail. At the feedpoint of the log-spiral antenna, the two electrodes are coupled to a few micrometer size metal-semiconductor-metal (MSM) interdigitated capacitor, having a square geometry. It functions as a photoconductive switch, since the

GaAs chip becomes slightly conducting in the region of the interdigitated capacitor when charge carriers are created by the laser light, followed by recombination with the emission of phonons, characterized by a measured time scale of $\tau_c = 500$ fs. The interdigitated capacitor fingers are about $1 \mu\text{m}$ apart. The dc-resistance of the photoconductive switch is typically of the order of $R_{sour,det} = 10\text{-}30 \text{ k}\Omega$ ¹¹ when the switch is closed, dependent on the charge carrier density, tuned by the laser power. For the electro-magnetic description of the photoconductive switch of the source and the detector, the characteristic wave impedance is much higher and amounts to $R_c^{S,D} \sim 140 \text{ k}\Omega$. It is estimated over the generated power in the frequency range used and the resulting current flow upon detection.¹⁷ We assume that the characteristic impedance contains no reactive components, which appears adequate to describe our experimental results.

The initially uncorrelated laser fields are coupled by the nonlinear, i.e. quadratic, dependence of the charge carrier creation in the GaAs (causing the frequency mixing). Detuning the DFB lasers by the frequency f , the impedance of the MSM interdigitated capacitor is modu-

lated by the same frequency. In other words, the switch is opened and closed on a timescale $\sim (2\pi f)^{-1} \gg (2\pi f_c)^{-1}$, which in our frequency range is much slower than the characteristic timescale $(2\pi f_c)^{-1} = \tau_c$ of the recombining carriers in the GaAs. Furthermore, the antenna impedance of the log-spiral circuit, $R_{ant} \approx 72 \Omega$,¹⁸ together with the photo-mixer capacitance C , defines an RC -time, which in our used frequency range is much shorter than the time period of the generated waves due to the frequency mixing, $RC \ll (2\pi f)^{-1}$.

Hence, together with the application of the dc-bias voltage, a THz current with frequency f oscillates in the MSM interdigitated capacitor and excites the log-spiral circuit. The log-spiral circuit has a counter-clockwise direction of turn in the propagation direction of the beam. Due to this geometry, it emits a left-circular polarized THz field through the silicon lens, indicated by the dashed red circle in Figs. 2(a) and (b). Sending the left-circular polarized THz field through the diagonal-horn antennas and the rectangular waveguide, shown in Figs. 2(a) and (d), the output field is linear polarized (red linear arrow at the output of the waveguide in Fig. 2(a)). The reason for this is the confined parallel-plate like geometry of the rectangular waveguide, shown in Figs. 2(a) and (d). In Fig. 2(d) the cut through the full-height rectangular waveguide indicates the hollow region with area $2b^2$ machined in the CuTe material. For the fundamental TE_{10} mode, this geometry only supports field lines perpendicular to the a-side and parallel to the b-side, hence, an electro-magnetic field with a linear polarization is characteristic for this waveguide mode. Due to the conversion from a circular-polarized to a linear polarized mode in the waveguide, the output power is lower by a factor 2. It is further decreased by additional, albeit small, waveguide losses when considering that the traveling distance through the waveguides with lengths $l = 39.6 \text{ mm}$ and $l = 79.2 \text{ mm}$ corresponds to many wavelengths ($\lambda \sim 1.2 \text{ mm}$) in our frequency range.

The detector is operated without applying a bias voltage to it and it is pumped by the same two DFB lasers through the beam combiner, like the source. This modulates again the impedance of the MSM interdigitated capacitor at the frequency f , but this time in the detector. The impinging THz electro-magnetic field on the detector is received by its log-spiral circuit and is characterized by an amplitude and phase which we obtain by post-processing using a Hilbert transformation of the real-valued detector photocurrent $I_{dc}(f)$, Eq. (1).

III. ELECTRO-MAGNETIC MODELING AND QUASI-OPTICAL PROPERTIES

The measured data will be compared with model-data in Fig. 6. Therefore, we describe first the electro-magnetic model which captures the full system. It is built from a separate analysis of the diagonal horn antennas (Sec. III A) and the rectangular waveguide (Sec. III B).

These separate parts are then combined to a full model of the assembled device, including the coupling to the source and the detector (Sec. III C). We use the standard ABCD-matrix formalism to obtain for each frequency the scattering parameter which subsequently can be compared to the measured transmission, cf. Fig. 6. The details of this approach are given below.

A. Diagonal-horn antenna

A three-dimensional finite element simulation of the diagonal-horn antennas has been conducted based on the CST software.¹⁹ The optimization of the antenna performance is achieved by varying the inner-conductor shape and length in the simulation. To obtain a compact device and to minimize the dissipative loss, a short antenna is favored, provided it has still a low enough return loss and reasonable quasi-optical beam properties. In the CST model the antenna design is built upon mesh cells, with the metallic boundary conditions imposed to define the electro-magnetic properties. The feedpoint (cf. Fig. 4, upper panel) has been implemented with an ideal impedance-matched waveguide port to minimize parasitic reflections. The waveguide port is also used as the excitation source for the simulation. The output (or input, when the antenna is employed as receiving device) of the diagonal-horn antenna is terminated by the free space impedance $Z_\infty = \mu_0 c_0$, with μ_0 being the vacuum permeability and c_0 the velocity of light in vacuum. A Vivaldi shape with a smooth transition to straight edges at the output, cf. Fig. 4 upper panel, yields a minimum input reflection $S_{11}(f)$ over the broad range of frequencies used in the experiment.

As a final step, we have included the designed antenna geometry in a three-dimensional construction model prepared in AutoDesk Inventor.^{20,21} Through this we achieve a one-to-one correspondence between the anticipated optical properties in the simulated diagonal horn antennas and the optical properties of the fabricated diagonal-horn antennas.

Our simulation results are summarized in Fig. 3. In the main figure we show the input impedance $Z_{11}(f)$, the inset shows $S_{11}(f)$ as a black solid line. Both quantities are referred to the feedpoint. Note the waviness of $Z_{11}(f)$ of the diagonal-horn antenna, which indicates a less than perfect match to the free-space impedance. The waviness can be reduced at the cost of a longer antenna with a smoother transition from the feedpoint waveguide to its output. As an illustration, we compare in the same figure the input impedance of the diagonal-horn antenna and the one of an input-matched rectangular full-height waveguide with the same dimensions as the antenna feedpoint. Obviously they follow the same trend, but the impedance function of the waveguide is smooth. These simulations take into account the conductor loss α_c of the diagonal horn and waveguide material CuTe (inset of Fig. 1).

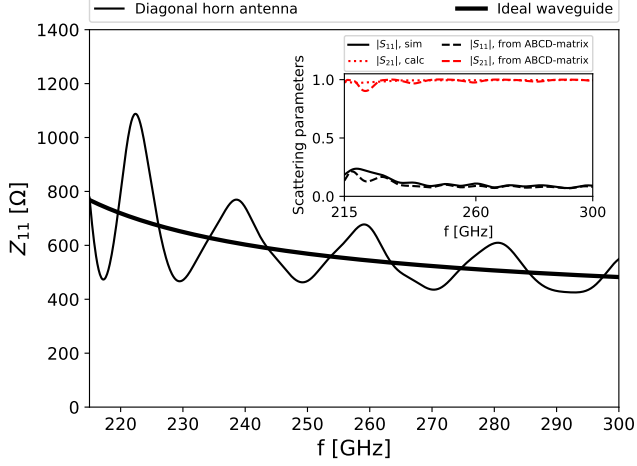


FIG. 3. Numerical 3D finite-element simulation results of the diagonal-horn antenna with rectangular waveguide-feed (Figs. 2(a) and (d) and Fig. 4), represented in terms of the input impedance $Z_{11}(f)$. For comparison, $Z_{11}(f)$ is shown also for an ideal impedance-matched rectangular full-height waveguide like sketched in Fig. 1(a). In the simulation, the diagonal-horn antenna is terminated in the free space impedance $Z_{\infty} = \mu_0 c_0$ and the waveguide is terminated by its frequency-dependent input impedance, representing the ideal impedance-match situation. The waviness in the result for the diagonal-horn antenna compared to the ideal waveguide result, shows the expected imperfection for our system when matching a rectangular waveguide via our diagonal-horn antenna to free space. The inset shows the simulated input reflection scattering parameter S_{11} and the resultant (calculated) scattering parameter S_{21} from the antenna feedpoint to its output as black solid and red short-dashed lines. The corresponding scattering-parameter pair derived from the ABCD-matrix formalism is shown for comparison as long-dashed lines.

We include the expected dissipative loss in the simulation for the diagonal-horn antennas, although it is known to be rather low in this antenna type. The reason is the advantageous field distribution,²² which drives surface currents parallel to the mechanical cut shown in Fig. 4. The calculated realized gain and the directivity in the antenna simulation is used to determine the antenna efficiency. From this a dissipative loss in the antenna of -0.53 dB in the center of the frequency band is found, small enough to approximate a reciprocal network. This approximation facilitates subsequent modeling. The input-reflection scattering parameter, $S_{11}(f)$, and the scattering parameter from the feedpoint to the antenna output, $S_{21}(f)$, can be expressed as,

$$\begin{aligned} S_{11}(f) &= |S_{11}(f)| \exp[i\theta(f)] \\ S_{21}(f) &= \sqrt{1 - |S_{11}(f)|^2} \exp[i\phi(f)] . \end{aligned} \quad (2)$$

In the equations, $\theta(f) = \arctan\{\text{Im}[S_{11}(f)]/\text{Re}[S_{11}(f)]\}$ is the argument of the complex-valued function $S_{11}(f)$ and $\phi(f) = \theta(f) + \pi/2 \mp n\pi$.²³ Due to the reciprocal-

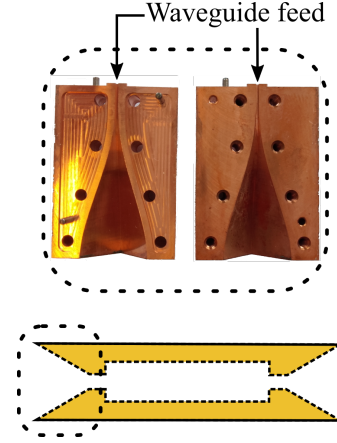


FIG. 4. Adjustment of the ideal model to the experimental situation. Diagonal-horn antenna opened along the E -plane (top). The microwave surface currents are induced parallel to this plane, i.e. perpendicular to the electric field. The bottom part of the figure sketches the cross-section through a diagonal horn antenna and waveguide assembly in which the waveguide channel is larger than the diagonal-horn antenna waveguide feedpoint. The interpretation of our measurements suggests such a configuration, which is in contrast to the ideal situation shown in Fig. 1(a).

network approximation, the Eqs. (2) describe the antenna as an emitting as well as a receiving device, $S_{21} \approx S_{12}$. For the back-to-back configuration shown in Fig. 1(a), S_{12} is the scattering parameter from the input to the antenna feedpoint for the receiving antenna, which connects to the waveguide. This means in particular, deriving S_{11} as a function of frequency is sufficient to determine the full set of scattering parameters for the diagonal-horn antenna.

Since the diagonal-horn antenna and waveguide device consists of three elements, a receiving diagonal-horn antenna, a rectangular full-height waveguide of length l and an emitting and identical output diagonal-horn antenna, we combine in Sec. III C the electro-magnetic properties of the three elements into a full model. A convenient way to achieve this is to exploit the ABCD-matrix formalism, which permits the combination of an arbitrary number of (two-port) microwave elements to calculate the full set of scattering parameters for the complete microwave elements assembly. The transformation between ABCD- and S -parameters for a two-port network with complex termination impedances is given by the matrix

elements²⁴

$$\begin{aligned}
A &= \frac{(Z_{01}^* + S_{11}Z_{01})(1 - S_{22}) + S_{12}S_{21}Z_{01}}{2S_{21}\sqrt{R_{01}R_{02}}} \\
B &= \frac{(Z_{01}^* + S_{11}Z_{01})(Z_{02}^* + S_{22}Z_{02}) - S_{12}S_{21}Z_{01}Z_{02}}{2S_{21}\sqrt{R_{01}R_{02}}} \\
C &= \frac{(1 - S_{11})(1 - S_{22}) - S_{12}S_{21}}{2S_{21}\sqrt{R_{01}R_{02}}} \\
D &= \frac{(1 - S_{11})(Z_{02}^* + S_{22}Z_{02}) + S_{12}S_{21}Z_{02}}{2S_{21}\sqrt{R_{01}R_{02}}}
\end{aligned} \tag{3}$$

and

$$\begin{aligned}
S_{11} &= \frac{AZ_{02} + B - CZ_{01}^*Z_{02} - DZ_{01}^*}{AZ_{02} + B + CZ_{01}Z_{02} + DZ_{01}} \\
S_{12} &= \frac{2(AD - BC)\sqrt{R_{01}R_{02}}}{AZ_{02} + B + CZ_{01}Z_{02} + DZ_{01}} \\
S_{21} &= \frac{2\sqrt{R_{01}R_{02}}}{AZ_{02} + B + CZ_{01}Z_{02} + DZ_{01}} \\
S_{22} &= \frac{-AZ_{02}^* + B - CZ_{01}Z_{02}^* + DZ_{01}}{AZ_{02} + B + CZ_{01}Z_{02} + DZ_{01}}.
\end{aligned} \tag{4}$$

In general, in the equations above every parameter is also a function of frequency which we include in our modeling. In addition, Z_{01} and Z_{02} are the complex termination impedances. The *-symbol indicates the complex conjugate and R_{01} and R_{02} are the real parts of the complex termination impedances.

By applying Eqs. (3) we find the frequency dependent ABCD-parameters of the diagonal-horn antenna from the previously determined set of S -parameters. In this calculation, $Z_{02} = Z_{\infty}$ is the free space impedance terminating the diagonal-horn antenna and $Z_{01} = (\omega/c_0)Z_{\infty}/\beta$, with ω the angular frequency and β the feedpoint waveguide complex propagation constant. We use first the nominal dimensions of the antenna's feedpoint waveguide to evaluate $\beta = \sqrt{(\omega/c_0)^2 - (\pi/a)^2}$, $a = 2b = 800 \mu\text{m}$. By back-transformation to the S -parameters using Eqs. (4), we evaluate the precision of this procedure in the inset of Fig. 3 (long-dashed lines) with the previously simulated S_{11} - and calculated S_{21} -parameter (solid and short-dashed lines). In general we find a satisfactory agreement for all frequencies, the agreement is better for increasing frequency. At the lowest frequencies the deviation amounts to at most 8%, accurate enough to permit a comparison to our experimental results.

B. Rectangular waveguide

The standard ABCD-parameters for the rectangular waveguide are²³

$$\begin{aligned}
A_{wg} &= \cosh(\gamma l) & B_{wg} &= Z_{01} \sinh(\gamma l) \\
C_{wg} &= Z_{01}^{-1} \sinh(\gamma l) & D_{wg} &= \cosh(\gamma l).
\end{aligned} \tag{5}$$

They take the same form as for the usual transverse-electro-magnetic (TEM) transmission line, like a coaxial cable. The only difference is the value of the complex propagation constant γ , due to the cut-off in the frequency spectrum of β and its frequency dependence, $\gamma = \alpha_c + i\beta$, with α_c and β as discussed above.

C. Complete setup and quasi-optics

Multiplying the ABCD-matrices of the single elements in the order as they appear in the setup shown in Fig. 1(a), i.e. receiving diagonal-horn antenna - rectangular waveguide of length l - emitting diagonal-horn antenna, one obtains the full ABCD-matrix of the setup. Using the relations in Eqs. (4) for the S -parameters, with $R_c^{S,D} = Z_{01,02} = 140 \text{ k}\Omega$ (Sec. II) the real-valued source and detection characteristic wave impedances, one obtains the total S -parameter set of the experimental setup, which should be proportional to the transmission we measure in the experiment.

Finally, we introduce the experimentally relevant Gaussian, i.e. quasi-optical, beam properties²⁵ of the source/detector and the diagonal-horn antenna, which is important in optimizing the experimental setup. First, the Gaussian beam profile of the source and detector are slightly asymmetric in their xz - and yz -planes, z being the propagation direction of the field shown in Fig. 1(a). This is quantified by the beam waist radii in these planes, $w_{xz} \sim 2 \text{ mm}$ and $w_{yz} \sim 2.2 \text{ mm}$ which are located at distances $\sim 25 \text{ mm}$ and $\sim 32 \text{ mm}$ from the aperture. The optical properties of the diagonal-horn antenna, although having slightly curved instead of linear slanted walls, is best approximated by the analytical theory by Johansson and Whyborn²². From their theory, we obtain for our diagonal-horn antenna design a waist radius of $w_{xz} = w_{yz} = 1.9 \text{ mm}$, a distance of $z_A = 14 \text{ mm}$ between the position of the beam waist and the aperture, as well as a Rayleigh length of $z_c = 9.6 \text{ mm}$. Additionally, the beam curvature at the aperture is characterized by the radius $R_A = 20.6 \text{ mm}$ and the beam waist at the aperture is $w_A \approx 1.77w_0$. For maximum optical coupling we arranged the photo-mixers and the diagonal-horn antennas such that the respective beam waists were on top of each other. Optimizing the position of the photo-mixers with respect to the diagonal-horn antennas has been achieved by moving them with micro-meter precision in order to maximize the photocurrent and to compensate for their aforementioned beam asymmetry.

IV. EXPERIMENTAL RESULTS AND ANALYSIS

The full results from the measurements and the model analysis for three different waveguides are presented in Fig. 6. Panel (a) (79.2 mm waveguide, experiment) and panel (b) (79.2 mm waveguide, model) are the transmission (proportional to S_{21}) as a function of frequency.

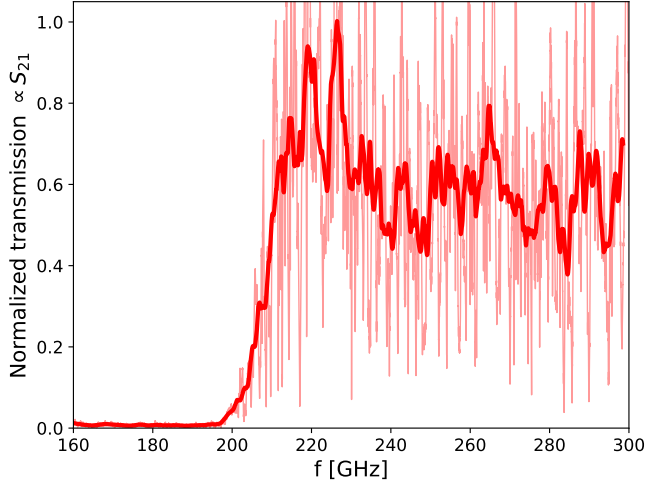


FIG. 5. Raw data (thin transparent line) to averaged data (thick line) processing for the case of the long-waveguide, cf. Fig. 6(a). In this case the raw data comprises six traces which were acquired subsequently and then averaged whereas the thick line is the result of the moving average post-processing procedure as described in the text.

Panel (c) and (d) show the results for the two short waveguides (39.6 mm), with panel (c) presenting the experiment and panel (d) the model. Obviously, all three waveguides become transmissive around 210 GHz (panels (a) and (c)), the anticipated by design waveguide cut-off. In addition, it is also clear that the two short waveguides show a very similar pattern as a function of frequency, short-period oscillations as a function of frequency. Thirdly, we also observe that the twice longer waveguide, panel (a), shows more variation in the transmissivity as a function of frequency than the two shorter ones. These variations occur on a much longer frequency scale than the features observed in the two shorter waveguides. To proceed towards a quantitative evaluation, which in the end will provide the communication rate of the waveguide, we address first some aspects of the data-processing (cf. also Fig. 5). It is followed by evaluating the deviations between the design-values of the waveguides and the actual realizations. We then comment on the observed differences over the full band (210-300 GHz), which we arbitrarily divided into 4 smaller sub-bands: 210-225 (i), 225-243(ii), 243-261(iii) and 261-300 (iv) GHz. Finally, we infer from these quantitative results the communication rate.

For the data presented in Fig. 6 the experimental and model results are both averaged, using a moving average post-processing procedure with an averaging length much smaller than the length of the data. The experimental data consist of six frequency-sweep datasets for the long waveguide and of two frequency-sweep datasets for each of the two short waveguides. The datasets for each waveguide were acquired subsequently and in the present analysis are averaged before the moving average post-processing procedure, cf. Fig. 5. In this way

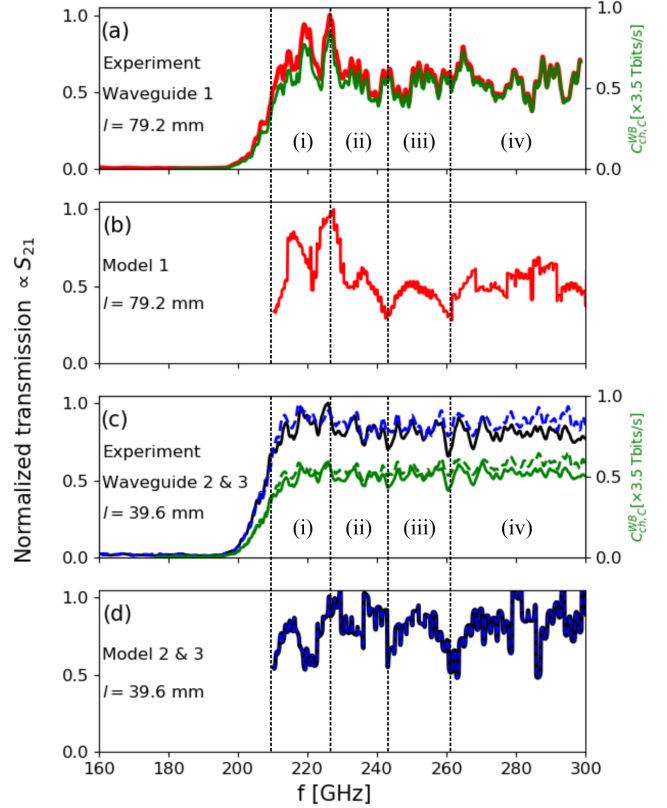


FIG. 6. Waveguide transmission measurements and modeling, expressed as instantaneous amplitude which is proportional to the scattering parameter from port 1 to port 2, S_{21} , cf. Fig 1(a). The transmissions (left y-axis) are normalized and by this referred to the waveguide input, neglecting a finite but small dissipative loss of the transmitted electro-magnetic waves. (a) and (c) show measurements of three different waveguides and two of these waveguides have the same length, shown in (c). (b) and (d) show modeling results for waveguides of two different lengths with $l = 39.6, 79.2$ mm used in the experiment. The wave transport through the waveguides with $l = 39.6$ mm and 79.2 mm is characterized by fundamentally different features over the measured frequencies and to explain this unambiguously, we label the data by sub-bands (i)-(iv), explained in more detail in Sec. IV. Note that the wave transport features are weaker for the short waveguides, (c), but that the most pronounced features are reproduced by the model in (d). The green traces in (a) and (c) summarize the calculated wideband coherent-state channel capacity [Eq. (8)] including the conductor loss. They are derived using the measured transmission, the power coupling factor determined by our model and an emitted power of $\sim 1 \mu\text{W}$ at 235 GHz, nearly constant over the other employed frequencies.

we smooth out fast fluctuations introduced by standing waves, caused by the large impedance mismatch between photo-mixers and diagonal-horn antennas. After this we normalize the data to enable a mutual comparison. The reason for this is that the setup shown in Fig. 1(a) determines essentially a relative transmission in comparison to the situation when no field is transmitted through the

waveguide. Unfortunately, a reference calibration procedure is generally difficult with this type of setup due to the sensitive optical alignment and the difficulty to measure absolute powers at these high frequencies. Nevertheless, the calculated S -parameters from the model permit an analysis of the absolute values of the signal loss of the transmitted field.

We find that in order to bring consistency between the measurements and the modeling results, we have to assume a smaller rectangular waveguide feedpoint of the diagonal-horn antenna, than the waveguide connecting the two diagonal-horn antennas (as sketched in Fig. 4). The most important experimental indication justifying this assumption is that for our three different waveguides, using the *same* diagonal horn antennas, we measure consistently the same onset of transmission, of about $f_{min} = 200$ GHz. Since the waveguide fabrication is not reproducible with this precision, for instance a deviation within the machining precision of $\pm 5\%$ of the waveguide a -side would shift f_{min} already by ± 20 GHz, this suggests that the rectangular waveguide feedpoint of the diagonal-horn antenna is the bottleneck for the transmission. Based on our measurements, it has to have a size of the order of $a = c_0/(2f_{min}) \sim 750 \mu\text{m}$. This corresponds to a deviation of $50 \mu\text{m}$ from the nominal design of $800 \mu\text{m}$ for the a -side introduced earlier and is consistent with the uncertainty expected from the waveguide machining. We assume, therefore, that the onset of transmission in all three waveguides is due to the size of the entry- and exit-orifice of the horn antennas.

Furthermore, in order to explain unambiguously the measured transmission spectrum we have to assume for the experimental waveguides slightly different dimensions than designed. For the long waveguide with length $l = 79.2$ mm a modified cross-section $a = 833.010 \mu\text{m}$. Similarly, for the shorter waveguides with lengths $l = 39.6$ mm a modified cross-section $a = 856.285 \mu\text{m}$. While choosing these new values for a in the waveguide, we keep in the model the diagonal-horn antenna feedpoint waveguide fixed to the nominal value of $800 \mu\text{m}$ for simplicity. In making the latter simplification, we accept a small underestimate of the input impedance of the diagonal-horn antenna, which turns out to be negligible for our analysis. Note that the decimal numbers of the a -values indicate the exact input we used for the modeling. Although the decimal numbers specify just a small length variation relative to the wavelength, slightly changing them modifies also the modeling results. This result is expected for a microwave device which is much longer than the wavelength and has a large impedance mismatch. It causes a sizeable standing wave ratio which is strongly influenced even by such small relative length variation, modifying the electric field amplitude at the detector. Additionally, we assume that the waveguides are shorter by in total about $11 \mu\text{m}$. This amounts to 4% of the height of the diagonal-horn waveguide flange which is mechanically squeezed during the mounting based on our experience, due to compression of the diagonal-horn antenna

waveguide flange using the screws shown on the clamp in Fig. 1(d) in the dashed area. This length modification has been included in our model through shortening the waveguide length l in Eqs. (5). With these adjustments the results shown in Fig. 6 can now be discussed including the comparison between experimental and modeled results.

As mentioned before, we divide the results for the transmission in four sub-bands 210-225 (i), 225-243(ii), 243-261(iii) and 261-300 (iv) GHz. This choice has no physical basis, but was suggested by the pattern observed in both the modeling and the experiment, in particular for the long waveguide. For this waveguide with length $l = 79.2$ mm, Figs. 6(a) and (b), the transmission shows three maxima in the regions (i) and (ii) and is slightly flatter in regions (iii) and (iv), but still showing pronounced features. All observed features in the measurement in (a) can be qualitatively and mostly also quantitatively related to the pattern found by the model shown in panel (b). However, the peak which we observe in the measurement between regions (ii) and (iii) is not found from the model. We assume that, given the large impedance mismatch between the photo-mixers and the diagonal-horn antenna, together with the overall length of the diagonal horn and waveguide device, much larger than the transmitted wavelength, that transmission features appear which are not exactly reproduced by our model. In this case the setup, but also the modeling, are very sensitive to small length variations, which would introduce similar features. We suggest that this is the most likely explanation for this particular transmission feature.

For the shorter waveguides of length $l = 39.6$ mm, the overall transmission is much flatter and shows less pronounced maxima in the spectrum. Similar to the long waveguide, the regions (i) and (ii) in the model for the short waveguide, Fig. 6(d), show three peaks. These can only be partly assigned in the measured transmission of waveguide 2, shown in Fig. 6(c), and of waveguide 3 shown in the same panel. The transmission of the latter one (blue-dashed line) compared to waveguide 2 (black solid line) shows generally a smoother frequency response with less pronounced features. In these waveguides, the transmission in the regions (ii) to (iii) is first slightly decreasing and then in region (iv) slightly increases again, separated from a small dip between region (iii) and (iv). At least this trend is reproduced by the model. This is clearly manifest for waveguide 2 for which also the dip is slightly deeper than for waveguide 3. In the latter case it is almost not distinguishable from the other ripples in the transmission. In region (i), the model predicts also a dip at around 220 GHz, which is not obtained in the measurement. Similar to the case for the long waveguide, we suspect here also the strong sensitivity to length variations of the waveguide, leading to standing wave patterns in the setup.

We like to add that the short period oscillations in the short waveguides are reminiscent of universal con-

ductance fluctuations (UCFs), studied earlier theoretically for light-scattering in waveguides.²⁶ In the latter work, the central outcome are correlation functions which quantify the coherence of the fluctuating intensity pattern of the light traveling through the waveguide, leaving out both inelastic scattering and absorption which have the effect of weakening or even destroying the coherence. The latter effects cannot be neglected in our case due to our normal conducting waveguides. Nevertheless, we built the auto-correlation function out of the raw data of the amplitude fluctuations measured in our short and long waveguides, and obtain a similar shape of the correlation function like derived in Feng *et al.*²⁶, in our case, however, as a function of frequency lag, Δf , instead of wavevector lag. We find that the amplitude auto-correlation functions for the short waveguides decay for $\Delta f = 492$ MHz to a value $1/e$, whereas for the long waveguide the same decay is already obtained for $\Delta f = 334$ MHz. The bare transmission between the two photo-mixers, i.e. without a waveguide in-between, shows also a fluctuating transmission, most likely due to internal reflections in the Si lens and standing-waves, and needs to be disentangled. In this case $\Delta f = 550$ MHz takes the largest value. Interestingly, we find that the cross-correlation between the amplitude fluctuations of two independent measurements of the two different short waveguides yields a non-vanishing correlation, about half as large as the auto-correlation, obtaining $\Delta f = 900$ MHz and suggesting a strong coherence between them. Cross-correlating in the same way the amplitude fluctuations measured in the long waveguide with the ones in the short waveguides, yields a much shorter coherence of $\Delta f = 200$ MHz and a much weaker correlation only about 17 % of the auto-correlation. As mentioned in Feng *et al.*²⁶, waveguides and microwaves are a versatile system to study UCFs, but concerning this aspect and the present status of our work, more work has to be done in the future.

Finally, we address the communication rate of these waveguides. We calculate, using the measured transmission, the expected communication rate through the waveguides, based on Eq. (8) of the next section. The results for the different waveguides are shown as green traces in the panels along with the experimental results in Figs. 6(a) and (c). To achieve these plots, the central challenge is to calculate the power P in Eq. (8) at the input of the waveguide. From our model we determine the electric-field coupling constant from the input to the output of the waveguide and the diagonal-horn antennas, i.e. S_{21} , and multiply it with the measured and then normalized transmission. Since the model accounts for dissipative losses, we obtain finally the absolute transmission. From this we calculate the power coupling and multiply it with the expected generated power at 235 GHz, about $1 \mu\text{W}$,^{11,15} taking into account the operation parameters of the THz source. Note that alternative direct and possibly absolute measurements of the power at these high frequencies are very difficult and often use the pyroelec-

tric effect.²⁷ This would introduce different uncertainties so that our procedure gives already a good enough estimate of the communication rate.

We finish the experimental section by comparing the possible communication rates we obtain, of the order of 1 bit per photon in the wideband coherent-state channel limit, with the limits derived by Caves and Drummond¹. We obtain this result using the theoretical framework described in Sec. V which also explains the assumptions used in our derivation. From their theory, the maximum communication rate expected for a coherent-state channel is of the order of 2 bits per photon. They find that this maximum rate can only be achieved by experimentally realizing the "one quantum - one bit - one mode" strategy we have mentioned in the introduction. This would be the case if $P/hf \sim C \sim f$. In our system, however, $P/hf \gtrsim C \gg f$. From this result, the implication for the practical realizable communication rate can be drawn from the analysis in Caves and Drummond¹. Our results imply that for our particular waveguide geometry, the injected power and used carrier frequencies, the rate at which quanta are transmitted down the channel is similar but still somewhat higher than the channel capacity and the carrier frequency is the slowest quantity. As a consequence, about one quantum per bit of information can be used, but far less than one bit per period (mode) is transmitted. This can be compensated by increasing the carrier frequency (at the same time reducing the waveguide dimensions to keep the single-mode character) and increasing the injected power P with the goal to realize the ideal "one quantum - one bit - one mode" communication strategy.

V. CHANNEL CAPACITIES

A rectangular waveguide, like shown in Fig. 1(a), is often viewed as a component in a receiver system, which guides a signal to a detector. Alternatively, it can be analyzed in information theory as a channel to guide information, which can be decoded with a minimal amount of error. In classical physics, noise is introduced by signal loss in the channel or by coupling loss, such as when the signal is injected into the channel from an emitter. If quantum mechanics plays a role, for example in the case of a coherent receiver, noise due to vacuum fluctuations has to be taken into account. For a signal carrier frequency f with bandwidth δf a noise power of $\sim hf\delta f$ will contribute. This contribution will be significant for signals with high-frequency carriers and a wide bandwidth of the order of $\delta f \sim f$. Both contributions, classical and quantum, have the effect of reducing the signal-to-noise ratio (SNR) at the receiver.

The physics of information theory has been formulated by Shannon,²⁸ creating the basis of quantum information theory.²⁹ The main interest is in the maximum rate at which information can be sent through a channel, while being still decodable without error. A quantitative mea-

sure is the maximum channel capacity C_{ch} , expressed in bits/sec. It is derived from the information entropy in the Shannon-theory through the source and channel coding theorems.²⁸ For the case of a lossless channel and a negligible thermal photon population, the classical channel capacity reads:^{1,28}

$$C_{ch,cl} = \delta f \log_2 \left(1 + \frac{P}{N\delta f} \right), \quad (6)$$

with P the transmitted power through the channel and N the noise power per Hz. In classical physics there is no lower limit on N , i.e. the noise can be infinitesimal small. Consequently, the channel capacity would tend to infinity. This unphysical result has motivated a number of theoretical studies to determine the proper physical limit of the channel capacity, reviewed by Caves and Drummond¹ and by Yuen and Ozawa³. For a quantum channel, cf. the later Eq. (9), Yuen and Ozawa³ derive in addition the limits of the average transmitted power P . Their work derives the maximum of the von Neumann information entropy, quantifying the maximum number of available input states to the channel, evidencing that it is classically an unbounded value but not quantum-mechanically. A heuristic method to impose a limit to $C_{ch,cl}$ is to state $N \sim hf$ so that,

$$C_{ch,C} = \delta f \log_2 \left(1 + \frac{P}{hf\delta f} \right). \quad (7)$$

The subscript C refers to a coherent state. The second part of the term between the brackets of Eq. (7) is then the mean photon occupation number, $\bar{n} = P/(hf\delta f)$, and the power P can be understood as a classical quantity. In this limit, Eq. (7) gives already the correct channel capacity for a free-space single coherent state channel with narrow bandwidth, $\delta f \ll f$. This expression yields a maximum capacity of ≈ 0.586 bits per photon. It can be determined by expressing Eq. (7) as a normalized capacity, $C_{ch,C} \rightarrow C_{ch,C}/(\delta f\bar{n})$, followed by finding its maximum.¹

In practice a wideband capacity is often relevant, for example, when many longitudinal modes are present within one transverse mode by frequency multiplexing. In this case, $\delta f \sim f$, and Eq. (7) is for a coherent state no longer valid, since $\bar{n} \ll 1$. Including the frequency dependence of the photon energy, Caves and Drummond¹ derived the wideband limit of the single frequency-multiplexed coherent state channel, yielding the capacity

$$C_{ch,C}^{WB} = \mathcal{A} \frac{1}{\ln(2)} \sqrt{\frac{2P}{h}}, \quad (8)$$

and, hence, $\mathcal{A} \times 2.0403$ bits per photon.

For a single number-state wideband channel, the channel capacity becomes

$$C_{ch,n}^{WB} = \mathcal{A} \frac{\pi}{\ln(2)} \sqrt{\frac{2P}{3h}}, \quad (9)$$

and yields, therefore, $\mathcal{A} \times 3.7007$ bits per photon. Equation (9) is determined by application of the so-called Holevo bound,^{1,30} which quantifies the maximal amount of information that can be obtained at the output of the channel using the concept of mutual information transfer. We like to add that the same Eq. (9) has been derived in Yuen and Ozawa³ by relaxing the finiteness assumptions in the Holevo bound and considering instead an infinite-dimensional input/output alphabet for the communication. A detailed discussion about the history of these approaches is given in Caves and Drummond¹.

The prefactor \mathcal{A} has to be determined separately for different types of waveguides and field-patterns. In Eqs. (8) and (9), $\mathcal{A} = 1$ for a free-space channel. For a full-height rectangular waveguide with dimensions $a = 2b$, cf. Figs. 1(a) and 2(d), one gets $\mathcal{A} = \cos(\theta_k)$. Moreover, $c_0 \cos(\theta_k)$ quantifies the reduction in longitudinal group velocity in the waveguide due to reflection at the waveguide walls (Giovannetti *et al.*² and Fig. 1(a)). The angle of reflection is given by $\theta_k = \arccos(k_z/|\mathbf{k}|)$ for the fundamental TE₁₀ mode, where $\mathbf{k} = (\pi/2a, 0, 2\pi/\lambda_g)$, with λ_g the wavelength in the waveguide. Note that the wavelength in the waveguide $\lambda_g > \lambda$ is always larger than the wavelength in free space, since $\lambda_g = 2\pi/\beta$ with $\beta = \sqrt{(\omega/c_0)^2 - (\pi/a)^2}$ the complex propagation constant. Consequently, $\theta_k \rightarrow \pi/2$ for long wavelengths approaching the waveguide cutoff $\lambda \sim 2a$, i.e. $\omega/c_0 \sim \pi/a$, where λ_g diverges and $\beta \rightarrow 0$, resulting in a vanishing group velocity, $(d\beta/d\omega)^{-1} = c_0\beta\lambda/2\pi$. In other words the channel capacity vanishes in this case since no information can be transmitted anymore.

This overview of formulas for the channel capacities demonstrates that the value depends theoretically on the type of waveguide. A convenient way to study the predictions of Eqs. (8) and (9) experimentally is to realize a frequency-multiplexed channel, which splits the available bandwidth into small non-overlapping frequency bins, which together carry a total transmitted power P . Furthermore, dependent on the type of channel, one has to realize the optimal photon-occupation number for each bin in order to achieve the maximum capacities (8) and (9). Optimal photon-occupation number distributions for the number-state and coherent-state channel are summarized in Caves and Drummond¹. For a single-mode waveguide like studied by us, each frequency bin represents then an independent longitudinal channel with different θ_k , within the same transversal mode, in this case the fundamental TE₁₀ mode.

In the practical case of a lossy waveguide, like in our experiment, illustrated by the black and red transmission curves shown in Fig. 1(b), not all photons of the electromagnetic field supplied at the input of the waveguide will reach the output. For the capacity of a number-state channel this creates a difficult theoretical problem related to the exact form of the input information entropy. This problem is explained in detail by Giovannetti *et al.*² and recently in Ernst and Klesse³¹ by considering a general quantum channel. This recent work studies as a proof-of-

principle the regularization of the maximum pure-state input-output fidelity of a quantum channel. We expect, that for the capacity of a quasi-classical coherent state channel, Eq. (8), reasonable conclusions are still possible even in the presence of loss. Therefore, we focus on this type of channel while conducting our experiment.

VI. FREE SPACE QUANTUM OPTICS EMPLOYING JOSEPHSON PHOTONICS AND WAVEGUIDES

This section addresses the conceptual framework of realizing free space quantum optics using recent achievements in Josephson photonics.^{32–41} In particular, the experimental works reported by Rolland *et al.*³² and Grimm *et al.*³⁵ implement an only battery-powered Josephson junction which is strongly coupled to a single mode, realizing a single photon source. The experiment in Westig *et al.*³⁸ reports two-mode amplitude squeezing below the classical limit using also an only battery-powered Josephson junction, but this time weaker coupled to two modes of different frequency. It is important mentioning that Grimm *et al.*³⁵ realized a NbN based Josephson junction that could in principle generate radiation in the frequency window employed in our work, extending the frequency range compared to only aluminum-based circuits.

For a given frequency and an adequate choice of the waveguide and diagonal-horn antenna dimensions, we like to recall that the waveguide cut-off wavelength scales as $\lambda_{min} \sim 2a$, with a being the long side of the rectangular waveguide and $b = a/2$ being the short side of the waveguide. It is then a straightforward microwave engineering task to excite a rectangular waveguide with a Josephson device by means of a planar antenna.⁴² The latter antenna design is compatible with co-planar waveguides frequently used in circuit quantum-electrodynamics. A second way to excite the fundamental waveguide mode in an even simpler way, but only working for lower GHz frequencies to about 60 GHz, uses a co-axial cable fixed in a back-short waveguide piece along the E -plane. For such a transition to work with low return loss, the co-axial cable inner core is fixed at a distance $\sim b$ away from the back-short and extending a distance $\sim b/2$ into the waveguide. The latter co-axial cable to waveguide transition is a standard and commercially available microwave element.

Connecting the aforementioned Josephson photonic devices in this way to the waveguide field, one takes advantage of the flexible way of generating tailored photonic fields in Josephson devices through strong charge-light coupling. At the same time one could radiate these fields into free space by means of the diagonal-horn antenna where quantum optic techniques provide to manipulate and measure the fields in a more flexible way than in a circuit configuration. For instance, for a free-space field one can then exploit additionally the polarization degree of freedom as reviewed in more detail by Sanz *et al.*^{43,44}.

Free-space ultra low-loss coupling to additional quantum devices, for instance to build a network, shows another benefit of this scheme.^{43,44} In order to minimize the signal loss in the immediate vicinity of the Josephson device, important to realize a number-state channel or to preserve a high degree of amplitude squeezing contained in a two-mode field, the rectangular waveguide should be made of a superconducting material or has to be coated with a superconductor up to a thickness much larger than the electro-magnetic penetration depth.

VII. CONCLUSION

To conclude, we have measured the transmission of different length rectangular full-height waveguides between 160 GHz and 300 GHz, connected to diagonal-horn antennas and optically coupled to a coherent detection scheme using a high-impedance source and detector with high dynamic range. A detailed but still simple enough electro-magnetic model includes the optical properties of the diagonal-horn antennas, the dispersion relations of the waveguides and the optical properties of the source and detector together with the coupling to those. The model accounts for most of the measured features. The central outcome of our measurements are highly-resolved transmission functions which reflect the frequency dependent impedance of the diagonal-horn and waveguide assembly, and the coupling mismatch to the source and the detector. A careful estimation of the channel capacity obtains a rate of 1 bit per photon in the wideband channel limit of a coherent state.

ACKNOWLEDGMENTS

We acknowledge funding through the European Research Council Advanced Grant No. 339306 (METIQUIM). We like to thank Michael Schultz and the precision-machining workshop at the I. Physikalisches Institut of the Universität zu Köln for expert assistance in the design and the fabrication of the diagonal-horn antennas and the waveguides. We also thank Anselm Deninger from TOPTICA Photonics AG, Germany, for extensive technical discussions. MW acknowledges the stimulating support from Katharina Franke and her group at the Freie Universität Berlin during the completion of this manuscript.

¹C. M. Caves and P. D. Drummond, “Quantum limits on bosonic communication rates,” *Rev. Mod. Phys.* **66**, 481–537 (1994).

²V. Giovannetti, S. Lloyd, L. Maccone, and J. H. Shapiro, “Information rate of a waveguide,” *Phys. Rev. A* **69**, 052310 (2004).

³H. P. Yuen and M. Ozawa, “Ultimate information carrying limit of quantum systems,” *Phys. Rev. Lett.* **70**, 363–366 (1993).

⁴H. Paik, D. I. Schuster, L. S. Bishop, G. Kirchmair, G. Catelani, A. P. Sears, B. R. Johnson, M. J. Reagor, L. Frunzio, L. I. Glazman, S. M. Girvin, M. H. Devoret, and R. J. Schoelkopf, “Observation of high coherence in josephson junction qubits mea-

- sured in a three-dimensional circuit qed architecture,” *Phys. Rev. Lett.* **107**, 240501 (2011).
- ⁵M. Reagor, H. Paik, G. Catelani, L. Sun, C. Axline, E. Holland, I. M. Pop, N. A. Masluk, T. Brecht, L. Frunzio, M. H. Devoret, L. Glazman, and R. J. Schoelkopf, “Reaching 10 ms single photon lifetimes for superconducting aluminum cavities,” *Applied Physics Letters* **102**, 192604 (2013), <https://doi.org/10.1063/1.4807015>.
- ⁶J. P. Turneaure and I. Weissman, “Microwave surface resistance of superconducting niobium,” *Journal of Applied Physics* **39**, 4417–4427 (1968), <https://doi.org/10.1063/1.1656986>.
- ⁷R. Barends, N. Vercruyssen, A. Endo, P. J. de Visser, T. Zijlstra, T. M. Klapwijk, P. Diener, S. J. C. Yates, and J. J. A. Baselmans, “Minimal resonator loss for circuit quantum electrodynamics,” *Applied Physics Letters* **97**, 023508 (2010), <https://doi.org/10.1063/1.3458705>.
- ⁸G. Chattopadhyay, I. Mehdi, J. Ward, E. Schlecht, A. Skalaré, and P. Siegel, “Development of multi-pixel heterodyne array instruments at sub-millimeter wavelengths,” (2004), IEEE Asia-Pacific Microwave Conference.
- ⁹H. Kazemi, D. Miller, A. Mohan, Y. Jin, M. Crawford, M. Wagenseil, and S. Long, “Ultra-compact g-band 16way power splitter/combiner module fabricated through a new method of 3d-copper additive manufacturing,” in *2015 IEEE MTT-S International Microwave Symposium* (2015) pp. 1–3.
- ¹⁰H. Bayer, “Considerations of a rectangular waveguide below cut-off piston attenuator as a calculable broad-band attenuation standard between 1 mhz and 2.6 ghz,” *IEEE Transactions on Instrumentation and Measurement* **29**, 467–471 (1980).
- ¹¹We use commercially available GaAs photomixers and the TeraScan 780 system from TOPTICA Photonics AG, Lochhamer Schlag 19, 82166 Gräfelfing/Germany. The source has the specification EK-000831 and the detector has the specification EK-000832. Further specifications are accessible in their online documentation, URL = <https://www.toptica.com>.
- ¹²S. Preu, G. H. Döhler, S. Malzer, L. J. Wang, and A. C. Gossard, “Tunable, continuous-wave Terahertz photomixer sources and applications,” *J. Appl. Phys.* **109**, 061301 (2011), <https://doi.org/10.1063/1.3552291>.
- ¹³E. R. Brown, “THz Generation by Photomixing in Ultrafast Photoconductors,” *International Journal of High Speed Electronics and Systems* **13**, 497–545 (2003), <https://doi.org/10.1142/S0129156403001818>.
- ¹⁴D. Saeedkia, ed., *Handbook of terahertz technology for imaging, sensing and communications* (Woodhead Publishing Limited, 80 High Street, Sawston, Cambridge CB22 3HJ, UK, 2013).
- ¹⁵A. Roggenbuck, H. Schmitz, A. Deninger, I. C. Mayorga, J. Hemberger, R. Güsten, and M. Grüninger, “Coherent broadband continuous-wave terahertz spectroscopy on solid-state samples,” *New Journal of Physics* **12**, 043017 (2010).
- ¹⁶D. W. Vogt and R. Leonhardt, “High resolution terahertz spectroscopy of a whispering gallery mode bubble resonator using hilbert analysis,” *Opt. Express* **25**, 16860–16866 (2017).
- ¹⁷Private communication with A. Deninger, TOPTICA Photonics AG, URL = <https://www.toptica.com>.
- ¹⁸K. A. McIntosh, E. R. Brown, K. B. Nichols, O. B. McMahon, W. F. DiNatale, and T. M. Lyszczarz, “Terahertz photomixing with diode lasers in low-temperature-grown gaas,” *Applied Physics Letters* **67**, 3844–3846 (1995), <https://doi.org/10.1063/1.115292>.
- ¹⁹CST - Computer Simulation Technology, URL = <https://www.cst.com>.
- ²⁰AutoDesk Inventor, URL = <https://www.autodesk.de/products/inventor/overview>.
- ²¹The construction model was used as blueprint for the micro-machining in the workshop of the I. Physikalisches Institut of the Universität zu Köln.
- ²²J. F. Johansson and N. D. Whyborn, “The diagonal horn as a sub-millimeter wave antenna,” *IEEE Transactions on Microwave Theory and Techniques* **40**, 795–800 (1992).
- ²³R. E. Collin, *Foundations for Microwave Engineering* (Wiley-IEEE Press, 1992).
- ²⁴D. A. Frickey, “Conversions between s, z, y, h, abcd, and t parameters which are valid for complex source and load impedances,” *IEEE Transactions on Microwave Theory and Techniques* **42**, 205–211 (1994).
- ²⁵P. F. Goldsmith, *Quasioptical Systems*, 1st ed. (IEEE Press, 445 Hoes Lane, Box 1331 Piscataway, NJ 08855-1331, 1998).
- ²⁶S. Feng, C. Kane, P. A. Lee, and A. D. Stone, “Correlations and fluctuations of coherent wave transmission through disordered media,” *Phys. Rev. Lett.* **61**, 834–837 (1988).
- ²⁷F. Sizov, “Terahertz radiation detectors: the state-of-the-art,” *Semiconductor Science and Technology* **33**, 123001 (2018).
- ²⁸C. E. Shannon, “A mathematical theory of communication, part i and part ii,” *The Bell System Technical Journal* **27**, 379 (1948).
- ²⁹C. H. Bennett and P. W. Shor, “Quantum information theory,” *IEEE Transactions on Information Theory* **44**, 2724–2742 (1998).
- ³⁰The original paper by A. S. Holevo⁴⁵ is written in Russian language and is strongly motivated in a rigorous mathematical framework. While we fully acknowledge his original work, we like also to refer to other research papers^{1,29,46,47} and a book chapter⁴⁸ which use and explain his original achievements. We feel that they provide a complete summary of his essential ideas in the framework of the state-of-the-art of quantum communication.
- ³¹M. F. Ernst and R. Klesse, “Regularized maximum pure-state input-output fidelity of a quantum channel,” *Phys. Rev. A* **96**, 062319 (2017).
- ³²C. Rolland, A. Peugeot, S. Dambach, M. Westig, B. Kubala, Y. Mukharsky, C. Altimiras, H. le Sueur, P. Joyez, D. Vion, P. Roche, D. Esteve, J. Ankerhold, and F. Portier, “Antibunched photons emitted by a dc-biased josephson junction,” *Phys. Rev. Lett.* **122**, 186804 (2019).
- ³³V. Gramich, B. Kubala, S. Rohrer, and J. Ankerhold, “From coulomb-blockade to nonlinear quantum dynamics in a superconducting circuit with a resonator,” *Phys. Rev. Lett.* **111**, 247002 (2013).
- ³⁴S. Dambach, B. Kubala, V. Gramich, and J. Ankerhold, “Time-resolved statistics of nonclassical light in josephson photonics,” *Phys. Rev. B* **92**, 054508 (2015).
- ³⁵A. Grimm, F. Blanchet, R. Albert, J. Leppäkangas, S. Jebari, D. Hazra, F. Gustavo, J.-L. Thomassin, E. Dupont-Ferrier, F. Portier, and M. Hofheinz, “Bright on-demand source of antibunched microwave photons based on inelastic cooper pair tunneling,” *Phys. Rev. X* **9**, 021016 (2019).
- ³⁶J. Leppäkangas, M. Fogelström, A. Grimm, M. Hofheinz, M. Marthaler, and G. Johansson, “Antibunched photons from inelastic cooper-pair tunneling,” *Phys. Rev. Lett.* **115**, 027004 (2015).
- ³⁷J. Leppäkangas, M. Fogelström, M. Marthaler, and G. Johansson, “Correlated cooper pair transport and microwave photon emission in the dynamical coulomb blockade,” *Phys. Rev. B* **93**, 014506 (2016).
- ³⁸M. Westig, B. Kubala, O. Parlavacchio, Y. Mukharsky, C. Altimiras, P. Joyez, D. Vion, P. Roche, D. Esteve, M. Hofheinz, M. Trif, P. Simon, J. Ankerhold, and F. Portier, “Emission of nonclassical radiation by inelastic cooper pair tunneling,” *Phys. Rev. Lett.* **119**, 137001 (2017).
- ³⁹J. Leppäkangas, G. Johansson, M. Marthaler, and M. Fogelström, “Nonclassical photon pair production in a voltage-biased josephson junction,” *Phys. Rev. Lett.* **110**, 267004 (2013).
- ⁴⁰J. Leppäkangas, G. Johansson, M. Marthaler, and M. Fogelström, “Input-output description of microwave radiation in the dynamical coulomb blockade,” *New Journal of Physics* **16**, 015015 (2014).
- ⁴¹A. D. Armour, B. Kubala, and J. Ankerhold, “Josephson photonics with a two-mode superconducting circuit,” *Phys. Rev. B* **91**, 184508 (2015).
- ⁴²M. P. Westig, K. Jacobs, J. Stutzki, M. Schultz, M. Justen, and C. E. Honingh, “Balanced superconduct-

- tor-insulator-superconductor mixer on a 9 μm silicon membrane,” *Superconductor Science and Technology* **24**, 085012 (2011).
- ⁴³M. Sanz, K. G. Fedorov, F. Deppe, and E. Solano, “Challenges in open-air microwave quantum communication and sensing,” in *2018 IEEE Conference on Antenna Measurements Applications (CAMA)* (2018) pp. 1–4.
- ⁴⁴M. Sanz, K. G. Fedorov, F. Deppe, and E. Solano, “Challenges in Open-air Microwave Quantum Communication and Sensing,” arXiv e-prints , arXiv:1809.02979 (2018), arXiv:1809.02979 [quant-ph].
- ⁴⁵A. S. Holevo, *Probl. Peredachi Inf.* **9**, 3 (1973), [Problems Inform. Transmission **9**, 177 (1973)].
- ⁴⁶A. S. Holevo and V. Giovannetti, “Quantum channels and their entropic characteristics,” *Reports on Progress in Physics* **75**, 046001 (2012).
- ⁴⁷J. Preskill, “Quantum Shannon Theory,” arXiv e-prints , arXiv:1604.07450 (2016), arXiv:1604.07450 [quant-ph].
- ⁴⁸P. Shor, “Quantum information theory: Results and open problems,” in *Visions in Mathematics: GAFA 2000 Special volume, Part II*, edited by N. Alon, J. Bourgain, A. Connes, M. Gromov, and V. Milman (Birkhäuser Basel, Basel, 2010) pp. 816–838.